Hybrid quantum repeaters with ensemble-based quantum memories and single-spin photon transducers

Gu, Fenglei; Menon, Shankar G.; Maier, David; Das, Antariksha; Chakraborty, Tanmoy; Tittel, Wolfgang; Bernien, Hannes; Borregaard, Johannes

DOI
10.1038/s41534-025-01119-5

Publication date
2025

Document Version
Final published version

Published in
NPJ Quantum Information

npj | quantum information

Article

Published in partnership with The University of New South Wales

https://doi.org/10.1038/s41534-025-01119-5

Hybrid quantum repeaters with ensemble-based quantum memories and single-spin photon transducers

Fenglei Gu[1], Shankar G. Menon[2], David Maier[1], Antariksha Das[1,3], Tanmoy Chakraborty[1,4], Wolfgang Tittel[1,5,6,7], Hannes Bernien[2,8,9] & Johannes Borregaard[1,10] ✉

Reliable quantum communication over hundreds of kilometers is a daunting yet necessary requirement for a quantum internet. To overcome photon loss, the deployment of quantum repeater stations between distant network nodes is necessary. A plethora of different quantum hardware is being developed for this purpose, each platform with its own opportunities and challenges. Here, we propose to combine two promising hardware platforms in a hybrid quantum repeater architecture to lower the cost and boost the performance of long-distance quantum communication. We outline how ensemble-based quantum memories combined with single-spin photon transducers, which can transfer quantum information between a photon and a single spin, can facilitate massive multiplexing, efficient photon generation, and quantum logic for amplifying communication rates. As a specific example, we describe how a single Rubidium (Rb) atom coupled to nanophotonic resonators can function as a high-rate, telecom-visible entangled photon source with the visible photon being compatible with storage in a Thulium-doped crystal memory (Tm-memory) and the telecom photon being compatible with low-loss fiber propagation. We experimentally verify that the Tm and Rb transitions resonate with each other. Our analysis shows that by employing up to nine repeater stations, each equipped with two Tm-memories capable of holding up to 625 storage modes, along with four single Rb atoms, one can reach a quantum communication rate of about 10 secret bits per second across distances of up to 1000 km.

The ability to transmit quantum information reliably between distant parties is a prerequisite for any useful application of a quantum internet[1,2]. The primary challenge to achieve this is the exponential attenuation of optical signals in fiber-based networks. To overcome this challenge, quantum repeaters have been proposed, where the distance is divided into shorter segments over which entanglement can be established in a heralded fashion. Once entanglement has been successfully established over the segments, entanglement swapping can extend the entanglement over the total distance[3,4].

Different quantum hardware, such as solid-state defect centers[5,6], atomic ensembles[7–9], trapped ions[10,11], rare-earth ions[12,13], and quantum dots[14], are currently being developed to enable a functional quantum repeater. There exist numerous theoretical proposals for repeater architectures tailored to the specific features of each hardware[15–18].

Quantum repeaters with ensemble-based quantum memories (QMs), pioneered by the Duan-Lukin-Cirac-Zoller protocol[19], have been pursued extensively experimentally due to their technological simplicity and multiplexing capabilities[20–22]. However, using ensembles makes it difficult to perform quantum logic on the stored information. Repeater protocols thus resort to probabilistic entanglement swapping schemes based on linear optics, severely limiting the performance. In addition, the probabilistic generation of approximate pairs of entangled photons from either the

[1]QuTech, Delft University of Technology, Delft, The Netherlands. [2]Pritzker School of Molecular Engineering, University of Chicago, Chicago, IL, USA. [3]ICFO - Institut de Ciencies Fotoniques, The Barcelona Institute of Science and Technology, Castelldefels, Barcelona, Spain. [4]Atomic, Molecular and Optical Physics Division, Physical Research Laboratory, Ahmedabad, India. [5]Department of Applied Physics, University of Geneva, Geneva, Switzerland. [6]Constructor University, Bremen, Germany. [7]Constructor Institute of Technology, Schaffhausen, Switzerland. [8]Institute for Quantum Optics and Quantum Information of the Austrian Academy of Sciences, Innsbruck, Austria. [9]Institute for Experimental Physics, University of Innsbruck, Innsbruck, Austria. [10]Department of Physics, Harvard University, Cambridge, MA, USA. ✉e-mail: borregaard@fas.harvard.edu

ensembles themselves or external Spontaneous Parametric Down Conversion sources leads to a fundamental trade-off between the rate and fidelity of the communication[23,24], severely limiting the usefulness of repeaters.

Quantum repeaters based on individual atoms or atom-like defects represent an alternative route[5,6,25]. Near-deterministic single-spin photon transducers, which can transfer quantum information between a photon and a single spin, can be achieved by coupling the atomic system to optical resonators, enabling efficient single-photon generation[26–28]. The ability to manipulate the hyperfine states of single atoms allows for quantum logic, enabling deterministic entanglement swapping and purification techniques[29]. However, repeater protocols based on merely individually trapped atoms make large multiplexing a formidable challenge, given current technology.

Here, we propose to combine ensemble-based QMs with single-spin photon transducers to enable a near-term hybrid quantum repeater with massive multiplexing, efficient photon generation, and near-deterministic entanglement swapping. In our scheme, a single-spin photon transducer is used for high-rate generation of entangled photon pairs, where, for each pair, one photon is to be stored in a multi-mode ensemble-based memory in a repeater node and the other is to be transmitted through a fiber to generate distant entanglement over the elementary segment between the nodes. Successfully entangled stored photons are read out from the memories, and near-deterministic entanglement swapping can be accomplished with the aid of extra single-spin photon transducers, thereby extending entanglement over neighboring elementary segments.

Furthermore, we outline a specific implementation with cavity-coupled single Rb atoms and Tm-doped crystal memories. We show how a single Rb atom coupled to two nanophotonic cavities with visible and telecom resonance frequencies, respectively, can function as a robust photon-pair source producing entangled visible and telecom photons. The telecom photon can propagate in standard optical fibers with minimum loss[30], and we experimentally verify that the visible photon is compatible with the resonance of the Tm-doped crystal. Thus, no frequency conversion is required for the repeater. We simulate the performance of the repeater for quantum key distribution (QKD) and show that rates of tens of secret bits per second over distances of up to 1000 km can be achieved with up to nine repeater stations, each containing only two ensemble-based memories and four single Rb atoms. Further increase of the rate is possible through additional multiplexing.

The article is organized as follows: Section II introduces the overall protocol and the mechanism of entanglement swapping. Section III discusses the mechanism by which Rb atoms emit both telecom and visible photons. Section IV presents an experimental study demonstrating the compatibility between the Rb photon source and QM based on Tm:$LiNbO_3$. In Section V, we show the simulation results of the repeater chain. Finally, Section VI offers a general discussion and an outlook.

Results

Structure of the repeater chain protocol

The general structure of the quantum repeater, composed of the single-spin photon transducers and ensemble-based QMs, is depicted in Fig. 1. The protocol is designed to distribute entanglement between two distant end nodes, Alice and Bob. It divides the total distance between Alice and Bob into multiple segments. In each segment, we use photon transducers to repeatedly emit entangled photon pairs on each side, storing one photon from each pair in the ensemble-based memories and attempting heralded entanglement generation over the segment with the other photons. Upon success, the now entangled photons are retrieved from the memories on each side and mapped into single-atom systems in a heralded fashion. This is followed by entanglement swapping using local Bell measurements to generate entanglement between Alice and Bob. The protocol thus consists of three main steps: entanglement generation, entanglement transfer, and entanglement swapping, as circled separately in Fig. 1.

For the initial entanglement generation step, as shown within the dashed red boundary in Fig. 1, two identical single-spin photon transducers are employed to produce entangled photon pairs continuously. For each photon pair, one of the photons is to be stored in the multi-mode ensemble-based QM while the other is sent via optical fiber to the middle station. At the

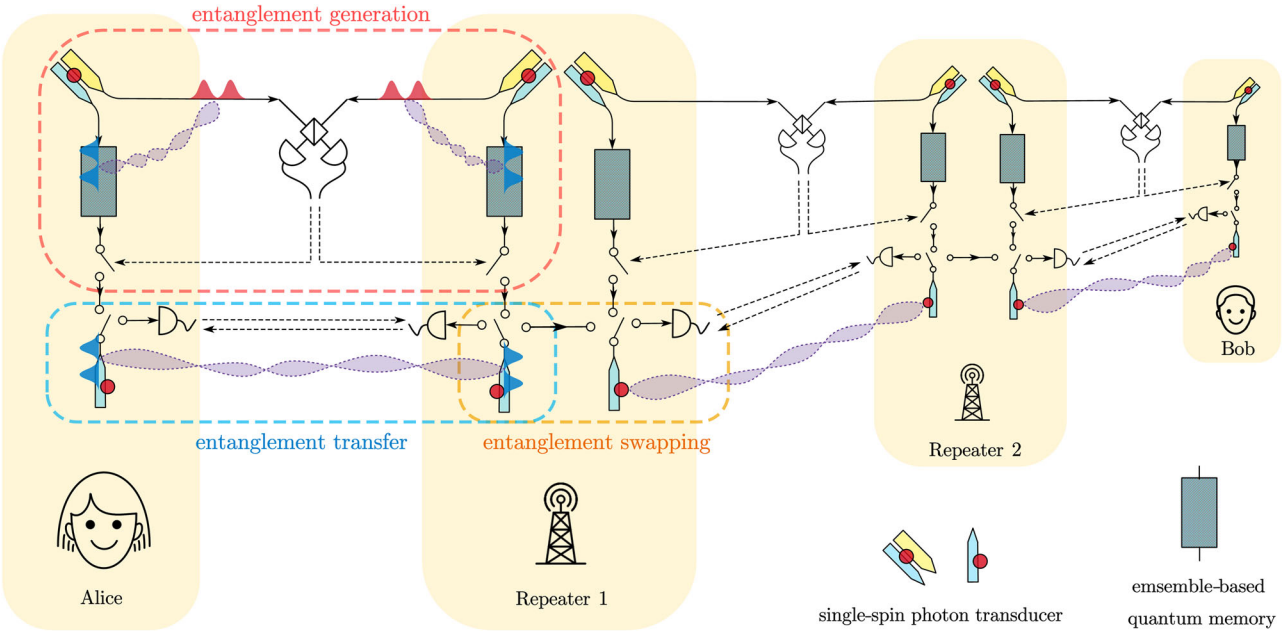

Fig. 1 | Structure of the quantum repeater chain architecture. The whole system contains two end nodes, Alice and Bob, connected by a series of repeater nodes. This figure depicts an example with two repeater nodes showcasing the key components involved. The yellow blocks represent the repeater nodes with the local devices depicted within. The protocol involves three main steps: entanglement generation, entanglement transfer, and entanglement swapping, as circled with dashed lines in different colors in the figure. The whole protocol harnesses two kinds of devices as the key components—the single-spin photon transducers and the ensemble-based quantum memories. The others are common devices, including 50-50 optical beam splitters, photon detectors, and optical switches, as sketched with conventional symbols in the figure. The solid-line arrows represent the optical fibers, and the dashed-line arrows the classical channels. Both the end nodes and the repeater nodes have symmetric layouts.

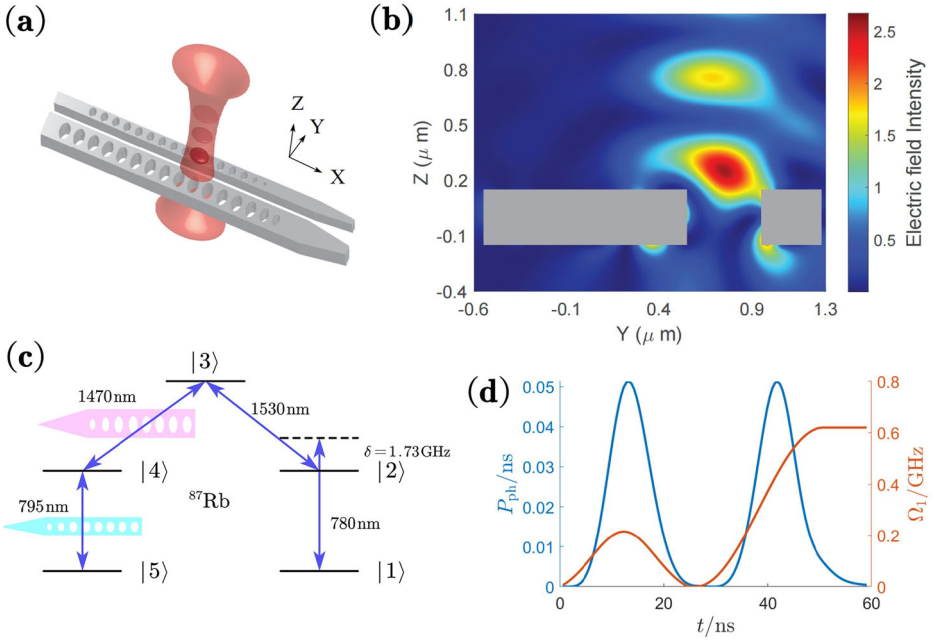

Fig. 2 | Rb emitter design and mechanism. **a** Parallel dual cavity design. The wide and narrow gray strips placed along the X direction represent the nanophotonic cavities resonant with the telecom and visible photons emitted from the Rb atom, respectively. They are of a TE mode telecom wavelength cavity (1470 nm) and a TM mode visible wavelength cavity (795 nm), both with a refraction index of 2.6 and a thickness of 300 nm. The light-red cone denotes the combination of the incident and reflected trapping lights, forming antinodes of high light intensity marked as dark red. The Rb atom is trapped in the nearest antinode to the cavities. **b** The slice of the simulated relative electric field intensity of the trapping light of the Z-Y plane centered around the trapping light position. It is normalized to the incident tweezer beam intensity. The two solid gray rectangles indicate the two nanophotonic cavities viewed from the X direction. **c** The intended driving path, from $|1\rangle$ to $|5\rangle$, in the Rb atom. The first two couplings are laser-induced, and the latter two are cavity-induced. There is a detuning $\delta = 1.73$ GHz respecting the $|1\rangle - |2\rangle$ energy difference in the first laser driving. **d** Temporal profile of the driving pulse of the first laser (orange) and emitted telecom and visible photons (blue). The code of this Rb-cavity system simulation can be found in ref. 103.

middle station, a linear optics Bell measurement is performed to entangle the photons stored in the QMs. While the success of this operation is probabilistic and subject to photon loss, information about which photon pairs were successfully entangled is sent back from the middle station to the nodes where QMs are located. The successfully entangled photons will be read out from the memories for further processing, while the failed ones will be discarded.

As illustrated in the area enclosed with the dashed blue line in Fig. 1, the successfully entangled photon pairs read out from the Tm-memories are transferred into the single-spin photon transducer systems. The entanglement is transferred from the photons to the spins by means of a cavity-mediated photon-spin gate[31–34], which also heralds successful retrieval of the photons from the ensemble-based memory and entanglement transfer to the spins. The gate operation leverages spin-dependent reflection from the cavity. In particular, for correctly tuned cavity parameters and a high cooperativity system, a photon will be reflected with/without a π-phase shift if the spin system is in a qubit state $|0\rangle/|1\rangle$. This enables a direct entangling operation between a time-bin encoded photonic qubit and the atomic spin qubit by applying a spin rotation in between the scattering of the early and late time bins. Subsequently, measuring the photonic qubit in the X-basis using a time-bin interferometer heralds the successful entanglement transfer from the photon to the atom[17,35].

The heralding signals are sent between the nodes to confirm the successful transfer. Once confirmed, the successfully entangled spins will be stored until entanglement swapping can take place with the neighboring link. Unsuccessfully entangled spins will be reset to attempt the next photonic transfer. Note that we employ separate spin systems for each memory to ensure that the unsuccessful retrieval of a photon from one memory does not influence the already successfully stored photon from the other.

Lastly, for the entanglement swapping between neighboring sections, one has to implement a Bell-state measurement between the two adjacent spins in one repeater node. This can be achieved in several ways using, e.g., a linear optics Bell measurement between photons emitted from both atoms or employing the same cavity-based spin-photon gate used for the entanglement transfer[35]. The latter allows us to surpass the 50% efficiency limit of a linear optics Bell measurement[36], and we therefore choose to focus on this. In this case, one of the atoms emits a time-bin photon entangled with its qubit states. This can be achieved through spin-dependent, pulsed excitation as recently demonstrated in ref. 37. The emitted photon is then scattered from the second cavity-atom system, implementing the same cavity-mediated entangling operation described above. A final detection of the photon in both spins in suitable bases completes and heralds the successful Bell measurement. The success probability of this operation is determined solely by the efficiency of the operations, which, in principle, can be almost deterministic.

Below, we outline a concrete implementation of this protocol with trapped single neutral Rb atoms and Tm-doped crystal QM (Tm-memory) and assess its performance.

Rb entangled-photon emitter and entanglement generation protocol

The Rb entangled-photon emitter consists of a single neutral Rb atom trapped with optical tweezers and coupled to two nanophotonic cavities, one with a resonance wavelength at 1470 nm and the other at 795 nm. There have been previous designs for two-mode cavity coupling of emitters with crossed cavities or using both TE and TM modes in a waveguide[38,39]. It is, however, challenging for such setups to maintain the required cavity quality factor while increasing the frequency separation of the two modes, which, in our case, corresponds to a wavelength difference of 675 nm.

Instead, we propose a parallel-cavity arrangement with the Rb atom located on the top of the two cavities, as shown in Fig. 2a. Such an architecture enhances the independence of the two cavities and is feasible by integrating atoms with on-chip nanophotonic cavities[40,41]. However, there are still many issues that need to be considered for choosing suitable system parameters. On the one hand, we need both cavities to be close enough to each other to reflect the tweezer light to form a stable trap for the Rb atoms[42,43]. In addition, placing the cavities closer to each other also provides larger atom-cavity coupling strengths, resulting in Purcell-enhanced emissions into the desired cavity mode. On the other hand, as the cavities of 1470 nm and 795 nm get closer, photonic modes can leak into each other, reducing the achievable quality factors.

We address these challenges by carefully selecting the material with the optimum refractive index, cavity separation, and cavity thickness. In our design, we chose silicon-enriched silicon nitride, SiN, as the cavity material

with a refractive index of 2.6. This selection enables better mode confinement compared to stoichiometric Si_3N_4, allowing for minimal separations between the cavities while maintaining high cavity quality factors. Similar cavities with high quality factors have been proposed and fabricated in silicon-enriched silicon nitride[44–46]. For practical fabrication considerations, both cavities are assumed to have a thickness of 300 nm. We perform simulations with a 1060 nm tweezer and 400 nm separation between the cavities and present the results in Fig. 2b. Our findings demonstrate that this design enables the 1470 nm telecom-photon cavity to achieve a quality factor of 1.4×10^5 with an average cooperativity of 34 with the Rb atom, while the 795 nm visible-photon cavity reaches a quality factor of 3.8×10^5 with an average cooperativity of 11. More details on the cavity design are provided in "Methods."

We will now describe in detail how this Rb-dual-cavity setup can function as a source of entangled photon pairs with the two photons at telecom and visible wavelengths, respectively. To achieve this, we harness five specific electronic orbital states from the ^{87}Rb atom. They are: $|1\rangle$:$5^2S_{1/2}|F=2, m_F=2\rangle$,$|2\rangle$: $5^2P_{3/2}|F=3, m_F=3\rangle$,$|3\rangle$: $4^2D_{3/2}, |F=3, m_F=3\rangle$,$|4\rangle$: $5^2P_{1/2}, |F=2, m_F=2\rangle$, and $|5\rangle$: $5^2S_{1/2}, |F=1, m_F=1\rangle$. Fig. 2c shows the coupling and driving of these five levels. In each photon emission cycle, we initialize the Rb atom in state $|1\rangle$ and drive it first to the $|2\rangle$ state with the first laser and then to the $|3\rangle$ state with the second laser. From the $|3\rangle$ state, the Rb atom will decay initially to the $|4\rangle$ state, emitting a photon into the telecom cavity mode (1470 nm), followed by another decay to the $|5\rangle$ state, emitting a second photon into the visible cavity mode (795 nm).

The second laser is continuously driving the transition $|2\rangle \leftrightarrow |3\rangle$ at a Rabi frequency of the same order as the cavity couplings; however, the Rabi frequency of the $|1\rangle \leftrightarrow |2\rangle$ drive is chosen to be about an order of magnitude lower. Besides, the pulse of the $|1\rangle \leftrightarrow |2\rangle$ drive is modulated with a pause in the middle of the driving process, as shown by the orange curve in Fig. 2d. The paused driving is calibrated such that the telecom and visible photons have equal probabilities of being both generated in the early time-bin (E) and the late time-bin (L), as shown by the blue curve in Fig. 2d. Ideally, this results in an entangled state of the form:

$$\psi_{vt} = \frac{1}{\sqrt{2}}\left(|\mathrm{E}\rangle_v|\mathrm{E}\rangle_t + |\mathrm{L}\rangle_v|\mathrm{L}\rangle_t\right), \tag{1}$$

where the subscripts refer to the visible (v) and telecom (t) photons. We note that the Rb atom is not entangled with the final photonic state and can repeatedly emit states of the form above. We simulated this emission procedure with the comprehensive Hamiltonian and parameters shown in Supplementary Note 1.

In each elementary segment, both end nodes are equipped with Rb emitters. The visible photons generated by the two Rb emitters are directly stored in QMs within the nodes, while the telecom photons are sent via optical fiber to a middle station. At the middle station, a beam splitter is used for erasing the which-way information, and photon detectors after the beam splitter are used to determine in which time bin the two photons arrive. In this way, with a maximum probability of 50% for the photon detectors to detect an early as well as a late photon, it ideally projects the two visible photons into a maximally entangled state

$$\psi_{vv} = \frac{1}{\sqrt{2}}\left(|\mathrm{E}\rangle_{vl}|\mathrm{L}\rangle_{vr} \pm |\mathrm{L}\rangle_{vl}|\mathrm{E}\rangle_{vr}\right), \tag{2}$$

where the subscripts "l" and "r" denote the left and right ends, and the ± sign is determined by whether the same detector (+) or different detectors (−) measure the photons in the early and late time bins. This allows one to realize the heralded entanglement generation in each segment in a multiplexed fashion. We emphasize that we assume this Bell measurement to be based on the detection of two photons, but we note that more efficient schemes in which only a single photon is detected exist[20]. This extension of our investigation is left to the future. We also stress that, unlike cascaded emission schemes for single-photon generation[47], our scheme does not suffer from a limitation on photonic interference due to the correlation of emission times between the optical and telecom photons. The precise detection of the telecom photons ensures the early-late time bin coherence of the optical photons, and any emission-time-dependent phase shift will lead to a global phase of the entangled pair.

In actual implementations, there will be imperfections and noisy processes in the above procedure[43]. To investigate the effect of these, we develop a detailed quantum optical model that includes the many-level structure of the Rb atoms, faulty laser polarization, finite and fluctuating cavity coupling, and various loss mechanisms. We refer to Supplementary Note 1 for details of this model and discuss only some of the key insights here.

Ideally, the first driving laser should drive only the σ_+ transitions. However, due to the device geometry, good polarization-maintained driving can only be obtained by driving with linear polarization. This results in an equal driving of σ_+ and σ_- transitions. The σ_- components leak population to many other hyperfine levels, as shown in Supplementary Note 1. This problem can, however, be mitigated by tuning the frequency of the first laser to match a specific resonance of a dressed state resulting from the continuous driving of the excited states from the second laser. The details of this method are presented in Supplementary Note 2.

Besides, the atoms will oscillate in the trapping potential due to finite temperature, which results in fluctuating cavity couplings. While this can, in principle, be mitigated by cooling the atomic motion[48–51], it is important to assess the robustness of our scheme to this.

Fluctuating cavity couplings mean that photons from different emitters will have varying amplitudes of the photonic time bins due to the fluctuations. This, in turn, will degrade the quality of the generated entanglement. While this cannot be completely circumvented, we identify certain "sweet spots" of the frequency of the first driving laser where the effect of these fluctuations can be efficiently suppressed. This can be understood from the dressed states of the subspace $\{|2\rangle, |3\rangle, |4\rangle\}$ coupled by the telecom cavity field and the second laser. By tuning the frequency of the first driving laser, we can target one of the dressed states such that the effect from the fluctuation of $|3\rangle - |4\rangle$ coupling will be counteracted by the effective $|1\rangle - |2\rangle$ coupling. This procedure is described in more detail in Supplementary Note 3.

Adopting the error-suppression techniques described above, our simulation shows that entangled states with an average fidelity of 0.98 with respect to the target state in Eq. (2) can be achieved. This simulation is based on fluctuating cooperativities of 34 ± 5.0 for the telecom-photon cavity and 11 ± 2.2 for the visible-photon cavity. For the polarization purity of the optical fields, our simulation shows that the first laser, second laser, telecom-photon cavity, and visible-photon cavity have polarization purities of 98%, 99%, 83%, and 67%, respectively. With these input parameters, our simulation shows that the Rb atom can emit telecom-visible photon pairs within ~60 ns, as shown in Fig. 2d. This is far shorter than the Rb state initialization time of roughly 1 μs. Hence we assume the Rb repetition rate to be $\nu_{eRb} = 1$ MHz.

Thulium-doped crystal quantum memory

In our proposal, multi-mode QMs require an ensemble-based approach[52,53]. Several possible methods exist, including electromagnetically induced transparency (EIT)[54], and photon-echo-related approaches[55], including the atomic frequency comb (AFC) protocol[56,57]. Relevant hardware includes alkaline atoms[58–62] and rare-earth-ion-doped crystals (REID crystals)[63–66]. While the transition of Rb vapor or laser-cooled Rb is naturally resonant with the emission wavelengths of photons from a single Rb atom, here we focus on the use of REID crystals in conjunction with the AFC protocol. The reason is three-fold.

First, in contrast with other memory protocols, as long as the bandwidth of the optical signal to be stored is smaller than certain atomic-level splittings, there is no trade-off between the bandwidth and the storage efficiency, nor between the number of the temporal modes that can be stored

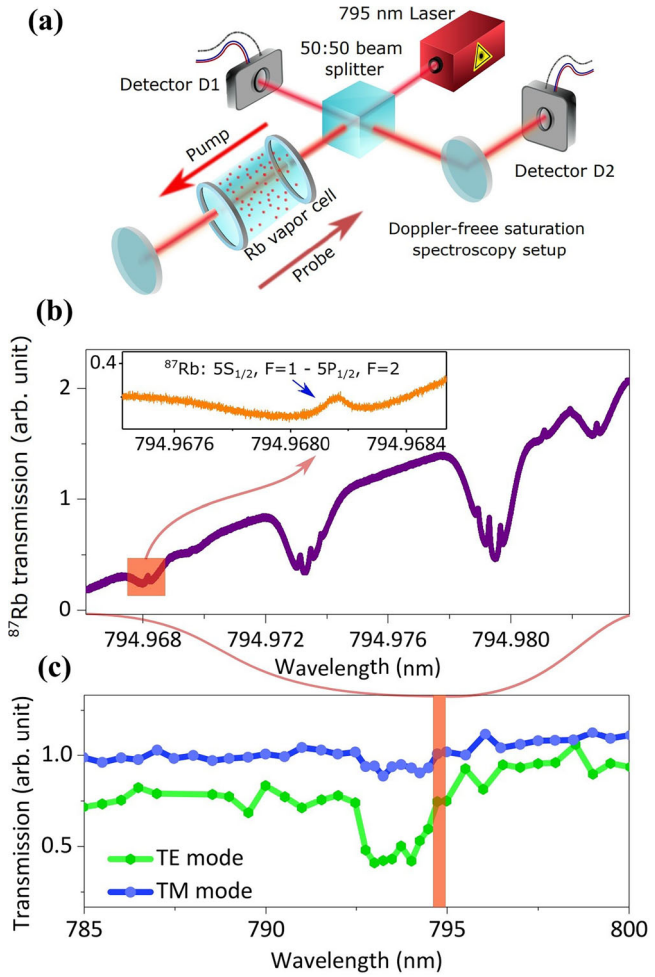

Fig. 3 | Compatibility of Rb and Tm- memory absorptions lines. a A simplified schematic of the Doppler-free saturation spectroscopy setup used to measure the absorption spectrum of rubidium. We use a laser with a continuously sweeping frequency, along with two light detectors (D1 to normalize the pump light, D2 to detect the probe light), to measure the absorption spectrum of the ^{87}Rb vapor. **b** Absorption spectrum of ^{87}Rb vapor. The inset shows an absorption peak corresponding to the $[5^2S_{1/2}, F=1] \leftrightarrow [5^2P_{1/2}, F=2]$ transition, which is used in our single-spin photon transducer. **c** The absorption spectrum of Tm:$LiNbO_3$. The orange bar indicates the wavelength range in (**b**), identifying the spectral overlap between the Tm-memory absorption and Rb photon transducer emission.

concurrently and the optical depth of the storage material [56]. This makes the AFC protocol directly compatible with the repeated emission of entangled photon pairs from the Rb-source described above. In fact, the multi-mode capacity is only limited by the total storage time and by the duration of each temporal mode; it can exceed 1000 temporal modes[22].

Second, another important point is that the 2-level AFC protocol in Tm-doped memory is noiseless, since atomic decoherence translates into a reduced readout efficiency rather than a reduction of the (post-selected) fidelity. However, for cold atoms, noise suppression techniques need to be incorporated to ensure high-fidelity operation.

Third, some Tm-doped crystals have matching resonance lines with ^{87}Rb, as shown in Fig. 3 with the example of Tm-doped $LiNbO_3$(Tm:$LiNbO_3$): We performed Doppler-free saturation spectroscopy[67] of the atomic ^{87}Rb vapor using an experimental setup schematically shown in a simplified form in Fig. 3a. A pump beam propagates through the ^{87}Rb vapor cell and turns into a probe beam after reflecting from a mirror passing through the ^{87}Rb vapor cell again. The intensities of both beams are detected by two photon detectors, respectively. This gives the transmission of the ^{87}Rb vapor as a function of the wavelength of the laser, i.e., the spectrum of the ^{87}Rb atom as shown in Fig. 3b. On the other hand, the transmission spectrum of a cryogenically cooled ($T \approx 600$ mK) Tm:$LiNbO_3$ crystal is depicted in Fig. 3c, showing spectral overlap with the ^{87}Rb spectrum. Specifically, we show an enlarged view of the $[5^2S_{1/2}, F=1] \leftrightarrow [5^2P_{1/2}, F=2]$ resonance line in the inset of Fig. 3b, which is used in our Rb single-spin photon transducer. Importantly, both spectra were taken simultaneously using the same laser and wavemeter. The resonance is therefore established free from calibration errors and ambient conditions that could, in principle, affect previously reported values.

Tm:$LiNbO_3$ has been used in several implementations of QM for light[68,69]. Ignoring spectral diffusion, which will be discussed below[70], and assuming sufficient optical depth, e.g., by using an impedance-matched cavity[71–74], the storage efficiency for photons at 795 nm wavelength is determined by the optical coherence time T_2 of its $^3H_6 \leftrightarrow {}^3H_4$ transition. More precisely, the normalized retrieval rate decreases as $R_{\mathrm{rtr}} \propto \exp(-4t/T_2)$, where t is the storage time, resulting in $t_{1/e} = T_2/4$. The coherence time itself is upper bounded by $T_2^{\max} = 2T_1$ where T_1 is the lifetime of the excited state—in the case of Tm:$LiNbO_3$, around 100 µs. Experimentally, a T_2 time of 117 µs has been reported at a temperature of 810 mK[75], which limits $t_{1/e}$ to around 30 µs. We note that other Tm-doped crystals with much longer coherence times are known. In particular, these include Tm:$Y_3Ga_5O_{12}$ (Tm:YGG), for which $T_2 = 1.1$ ms has been measured at 500 mK[9,76]. In addition to coherence time, spectral diffusion is another factor that can limit the possible storage time[9,70,75–79]. However, there are several ways to mitigate the effect of spectral diffusion, including so-called zero first-order Zeeman transitions[80,81], a reduction of the temperature[75,78], or co-doping with other ions[82,83]. For the simulations in this paper, we assume that the storage efficiency is only determined by the coherence time, which we further assume to be given under optimized experimental conditions by its upper limit of $2T_1$. In the case of Tm:YGG, we thus find $R_{\mathrm{rtr}} \propto \exp(-4t/2.6\mathrm{ms})$. In addition, taking a maximum storage bandwidth at $B = 1T$ of around 50 MHz into account[81] (the bandwidth is limited by atomic-level splitting that determines the emergence of additional absorption features during the creation of the AFC), we calculate a temporal multiplexing capacity of around 10000.

As shown in Fig. 3, the $^3H_6 \leftrightarrow {}^3H_4$ transition line of Tm:$LiNbO_3$ spectrally overlaps with the $[5^2S_{1/2}, F=1] \leftrightarrow [5^2P_{1/2}, F=2]$ line in ^{87}Rb. However, the same line in Tm:YGG is slightly off-resonant (the Rb transition is centered at 794.97 nm and features a linewidth of $2\pi \cdot 5.7$ MHz while the line of a 1% doped Tm:YGG crystal is centered at 795.32 nm with 56 GHz linewidth[84]). However, crystal engineering, e.g., by co-doping[82,83], may solve this problem. Experiments show that a linear increase of the inhomogeneous linewidth in Tm:$Y_3Al_5O_{12}$(Tm:YAG) can be induced, for example, by 24 GHz/Scandium%[85] and by 3.6 GHz/Europium%[86] without detrimentally affecting the coherence properties of the crystal. It is reasonable to assume that these methods work for Tm:YGG as well. While more work remains to be done, it therefore appears feasible to match the Rb line with the absorption line of a Tm-doped crystal, allowing the creation of QM for light with the desired specifications.

Simulated performance of the repeater chain

To assess the performance of the quantum repeater chain, we carry out Monte Carlo-based simulations to evaluate the achievable secret key rate in the context of QKD. Each simulation involves multiple independent realizations of the stochastic behavior of the repeater chain. A single realization proceeds iteratively: in each iteration, events such as entanglement generation, transfer, swapping, and end-node measurement are simulated with the time of each event sampled from their corresponding probability distributions. A realization terminates either when 100 successful end-to-end entanglements are established or when 10,000 iterations have been completed.

For the ith realization, we record the total distribution time T_i and the number of successful end-to-end entanglements n_i established during that time. This yields an estimate of the average entanglement distribution rate, defined as $R_i = n_i/T_i$.

Table 1 | System parameters assumed in simulations of the hybrid repeater chain

Rb emitter repetition rate (ν_{eRb})	1 MHz
Tm-memory typical photon preserving time (T_2/4)	0.65 ms
fiber attenuation rate	0.2 dB/km
light (classical signal) speed in fiber	2×10^5 km/s
fiber-cavity coupling efficiency (η)	0.95
entanglement transfer efficiency	0.95
entanglement swapping efficiency	0.92
entanglement swapping time	200 ns
photon detection efficiency	0.99
initial entangled photonic state (ρ_0) fidelity	0.98
operational error per repeater node (ϵ)	10^{-3}, 10^{-2}, 10^{-1}
Rb spin-memory storage cut-off time (t_{cut})	10 ms
Rb spin-memory coherence time (T_{mRb})	1 s

Several parameters influence R_i. The repetition rate of the Rb emitter is set to $\nu_{eRb} = 1$ MHz, and the fiber attenuation rate is 0.2 dB/km with the speed of light in the fiber assumed to be $c = 2 \times 10^5$ km/s, which determines the time of classical communication between the repeater stations. The retrieval efficiency of the Tm-memory, which depends on the storage time t, is

$$R_{rtr} = \eta^2 \exp\left(-\frac{4t}{2.6\,\text{ms}}\right), \tag{3}$$

where $\eta = 0.95$ is the assumed coupling efficiency to/from the fiber to the memory.

The entanglement transfer efficiency is assumed to be 0.95, primarily limited by photon loss in the optical circuit. The entanglement swapping efficiency is assumed to have an operation time of 0.2 μs and a success probability of 0.92. This results from a photon emission efficiency of 0.97 from one Rb atom (assuming a cooperativity of 30) and an entangling efficiency of 0.95 with the partner atom, the same as the entanglement transfer efficiency.

Lastly, the single-photon detection efficiency is taken as 0.99. Photon detection plays a role in entanglement generation, transfer, swapping, and the final measurements at the end nodes.

To model the decoherence affecting the evolution of the quantum states, we assume a depolarizing channel. For each of the n_i successful entanglement distributions in realization i, the final density matrix of the entangled qubits shared by Alice and Bob is described by

$$\rho_j = P_j\,\text{Bell}_{N-1}(\rho_0^{\otimes N}) + \frac{1}{4}(1 - P_j)I, \tag{4}$$

where ρ_0 (fidelity 0.98) is the estimated density matrix of an elementary link entangled state, shown in Supplementary Note 1, and N is the number of distance segments divided by $N-1$ repeater nodes. The operator $\text{Bell}_{N-1}(\cdot)$ denotes $N-1$ perfect Bell-state measurements. The coefficient P_j is defined as

$$P_j = (1-\epsilon)^{N-1} \exp\left(-\frac{\sum_k^{2(N-1)} \tau_k^j}{T_{mRb}}\right), \tag{5}$$

where ϵ quantifies the cumulative error per repeater station due to quantum-state operations of entanglement transfer and swapping. We consider values $\epsilon \in \{10^{-3}, 10^{-2}, 10^{-1}\}$. The set $\{\tau_k^j\}_k$ represents the sampled waiting times of the $2(N-1)$ qubits involved in Bell-state measurements. A memory cut-off policy is enforced such that $\tau_k \le t_{cut} = 10$ ms (optimized). The memory coherence time is assumed to be $T_{mRb} = 1$ s. End-node qubits are assumed to be measured immediately upon arrival and are not subject to storage decoherence. To provide a concise overview of the different parameters assumed in our simulation, we summarize them in Table 1.

For each repeater configuration, characterized by a total distance L and a number of repeater stations $N_{rep} = N-1$, we simulate 100 independent realizations. The final estimate of the average entanglement distribution rate is

$$R_{suc} = \frac{1}{100}\sum_{i=1}^{100} R_i, \tag{6}$$

and the final estimated density matrix is given by

$$\rho = \frac{\sum_{i=1}^{100}\sum_{j=1}^{n_i}\rho_{i,j}}{\sum_{i=1}^{100} n_i}. \tag{7}$$

From the final state ρ, we derive the average quantum bit error rates for both Z- and X-basis measurements:

$$Q_Z = 1 - \langle 00|\rho|00\rangle - \langle 11|\rho|11\rangle, \tag{8}$$

$$Q_X = 1 - \langle ++|\rho|++\rangle - \langle --|\rho|--\rangle, \tag{9}$$

where $|0\rangle$ and $|1\rangle$ are the computational (Z-basis) states, and $|\pm\rangle = \frac{1}{\sqrt{2}}(|0\rangle \pm |1\rangle)$ are the X-basis states of the qubits held at the end nodes.

Based on the BB84 protocol[87], we estimate the raw secret key rate as

$$R_{SK} = \max\big(0,\ 1 - H(Q_X) - H(Q_Z)\big) \times R_{suc}, \tag{10}$$

where $H(\cdot)$ denotes the binary entropy function. While the original BB84 protocol includes a factor of 1/2 due to random basis choices, this factor can be omitted in the asymptotic limit of infinitely long keys without compromising security[88,89].

In addition to the baseline configuration where each end of a segment uses a single Rb photon transducer for qubit storage (as illustrated in Fig. 1), we also simulate scenarios incorporating multiple (N_{mRb}) Rb photon transducers per end. This second level of multiplexing enhances the entanglement swapping efficiency.

Figure 4 presents the simulated average secret key rate R_{SK} as a function of total distance L, for various values of N_{mRb} and operational error per node, ϵ. For each configuration, we optimize the number of repeater stations N_{rep} and the memory cut-off time t_{cut} to maximize the per-segment secret key rate, defined as R_{SK}/N. Across all simulations, we find that a cut-off time of $t_{cut} = 10$ ms is near-optimal for an Rb spin coherence time of $T_{mRb} = 1$ s. The optimal value of N_{rep} used in each data point of Fig. 4 is reported in Supplementary Note 4.

Our results show that secret key rates on the order of 10 bit/s and 1 bit/s can be achieved over a distance of 1000 km for entanglement swapping error rates of $\epsilon = 10^{-3}$ and $\epsilon = 10^{-2}$, respectively. These results assume that Tm-memories have sufficient multiplexing capacity to support continuous repeater operation. Specifically, the required number of memory modes is given by

$$N_{mod} = \nu_{eRb} \cdot \frac{L}{N \cdot c}, \tag{11}$$

where ν_{eRb} is the photon generation rate, or the repetition rate of a single Rb emitter, and c is the speed of light in the fiber. Depending on the total distance and the optimal repeater configuration, N_{mod} ranges from 167 to 1000 in the simulations, which falls within the capabilities of rare-earth-doped QMs. Further increases in the secret key rate could be achieved by deploying additional Rb atoms as photon emitters to enhance the photon generation rate ν_{eRb}. We also performed simulations with a more modest operational error per node of 10% to reflect more near-term experimental

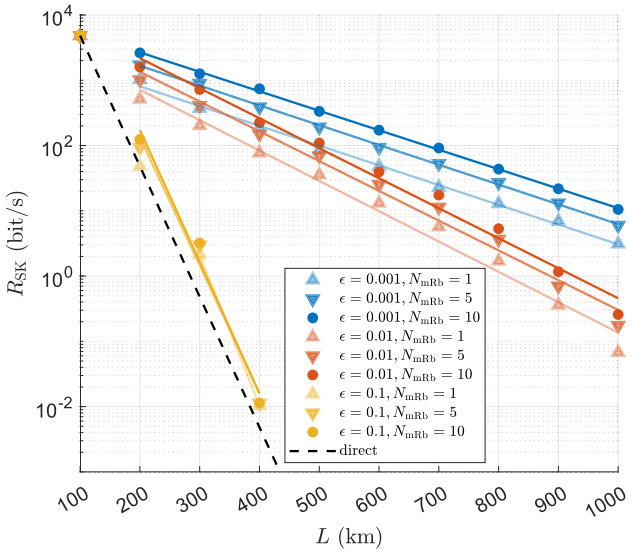

Fig. 4 | Average secret key rate (R_{SK}) as a function of distance (L) for different entanglement swap error probability (ϵ), and number of auxiliary Rb memory atoms (N_{mRb}). Note that the total number of Rb memory atoms in each repeater station is $2N_{mRb}$. The dashed black line presents the secret key rate with no repeaters but only a direct link between the two end nodes. The solid lines are linear fits excluding the data points for $L = 100$ km. The optimal number of repeater stations corresponding to each data point can be found in Supplementary Note 4. The simulation code is available in ref. 103.

implementations. Due to the error build-up across the repeater chain, such high operational errors limit the achievable distance to a few hundred kilometers and a single repeater node. However, we still observe a fourfold increase in the rate compared to direct transmission.

Discussion

In summary, we have proposed a hybrid quantum repeater employing single-spin photon transducers and ensemble-based photonic memories to achieve a high-rate entanglement distribution over large distances. The hybrid architecture directs the massive multiplexing necessary for battling transmission loss in the optical fibers to the ensemble-based memories, while efficient and near-ideal photon pair generation and entanglement swapping are enabled by the single-spin photon transducers. Furthermore, we provided a specific example that utilizes Rb atoms coupled to nanophotonic cavities as single-spin photon transducers and Tm-doped crystals as ensemble-based memories for massive multiplexing.

Our simulations showed that operational errors at the %-level per repeater node are required to reach long distances. Although past experimental demonstrations of cavity-mediated spin-photon gates with atomic systems have been limited to fidelities of ~80%[90,91], nanophotonic cavities, as considered here, or fiber-based cavities have demonstrated more than an order of magnitude higher cooperativities of the atom-cavity system[43,92]. This shows the promise of such platforms to reach significantly higher fidelities comparable to similar gate operations with strongly coupled solid-state defect centers, where fidelities >95% have been achieved[31]. Additionally, employing more complex operations such as entanglement purification techniques[29] to boost the fidelity could be envisioned through the quantum logic enabled by the single-spin photon transducers.

The overall framework presented here is relevant to other combinations of hardware besides the specific example analyzed in this work. Efficient single-spin photon transducers can be realized with diamond defect centers[6] and quantum dot systems[93], which can be matched with other ensemble-based memories based on AFC[56], Raman[94], or EIT[54] storage using impurity-doped crystals[66,95] or atoms, either laser-cooled or at room temperature. We note that different hardware combinations may require frequency conversion to be compatible, which can be achieved through standard techniques based on non-linear waveguides[6,30,96,97]. We have focused on the combination of the Rb entangled photon source with Tm-doped crystal memories due to their significant multiplexing potential. However, another interesting extension of this work would be to consider the combination of the entangled photon source with cold Rb atomic ensembles[98] in our repeater framework.

While combining different hardware is arguably more complex than a single hardware repeater, the overall requirements for reaching high-rate entanglement distribution may be substantially relaxed, as demonstrated in this work. We thus believe that further investigations of hybrid repeater architectures where ensemble-based memories are combined with single quantum emitters are a promising direction for future work.

Methods

Trapping and cavity designs

To couple an atom with two cavity fields, we design two nanophotonic cavities at the target frequencies fabricated parallel to each other, combined with a trap geometry that enables trapping an atom between the cavities. The individual cavities are designed by quadratic tapering of the filling fractions on a nanobeam waveguide[99]. For practical fabrication considerations, both cavities are designed with the same thickness. Due to its larger wavelength, the TE cavity at 1470 nm, requires a larger thickness for mode confinement and subsequently a high quality factor. However, for TE mode cavities for 795 nm, these thicknesses result in low modal overlap in the atom trapping region due to large mode confinement. To overcome this issue, we make use of the TM mode cavity design for the 795 nm cavity, which requires a larger thickness while maintaining decent modal overlap in the trapping region.

Quality factors of both the 780 nm and 1470 nm cavities are individually optimized and brought close to each other to form a stable trap geometry. Atoms can be trapped near similar nanophotonic devices by bringing the tweezer adiabatically on top of these devices and trapping the atom in lattices formed by the incident and reflected tweezer[40,42,100]. In the case of two parallel cavities, trapping on top of any one of the two cavities results in minimal coupling to the other cavity due to a minimal cavity mode at the trapping region. To have a significant coupling strength to both cavities, we propose trapping in between the two devices as an alternate implementation. If the separation between the parallel cavities is larger than the wavelength and the diffraction-limited spot size of the trapping tweezer, atoms can be trapped in the normal tweezer. However, the large Rayleigh range of a normal tweezer implies an atomic wave function larger than the device's thickness. This results in a large variation in the cavity coupling strength experienced by the atom from shot to shot. To overcome this, we restrict the separation between the two parallel cavities to be significantly less than the trapping tweezer wavelength. In this case, the incident tweezers beam is reflected by the combined device structure to form a lattice-like potential similar to a single device case. For a reasonable trapping potential of atoms, the separation between the devices should be smaller than half the trapping tweezer wavelength.

While the cavities were designed to have high quality factors individually, when they are kept next to each other, the mode from one cavity can leak into the other. These additional extrinsic losses κ_{ext} through the second waveguide result in lower overall quality factors ($Q = \frac{\omega}{\kappa_{ext}+\kappa_{int}}$; ω is the resonant frequency; κ_{int} is the intrinsic losses not coupled into any waveguides; κ_{ext} includes losses into the intended waveguide mode and the additional losses to the nearby waveguide). This loss is a function of the separation between the two cavities, where the loss increases with reduced separation between the cavities.

We iterate between device separation, thickness, and refractive index of the material to find a deep trap potential while maintaining high quality factors required for the results presented in the paper. To iterate over the refractive index, we assume tuning of the silicon enrichment ratio in the silicon nitride. However, the ratio of silicon in the silicon nitride also modifies the bandgap of the material. As the nitride content is reduced, the refractive index and the bandgap approach that of bare silicon[101]. To avoid the above bandgap excitation using the 780 nm laser involved in the

protocol, we assume the refractive index of 2.6, as assumed in the paper, results in a bandgap larger than 1.6 eV.

Atoms can be trapped in regions where cavity fields have predominantly linear polarization direction on top of nanophotonic devices[102]. However, moving the trap to the edge of the devices results in cavity field polarization to have components in more than one dimension in the trapping region, without specific control over the phase between the polarizations. This results in varying proportions of contributions from σ_+, σ_-, and π in the trapping region. The purity of the intended sigma polarization is marked in Fig. 1 of Supplementary Note 1. To overcome this issue, we make a careful selection of the states involved in the scheme. The level scheme involved in the protocol is chosen in a way that, under correct excitation, only σ_- polarization of the cavity fields couples between atomic states. The corrections coming from the faulty excitation are labeled in the figure and are accounted for.

Data availability

Data and codes can be available from the corresponding author upon reasonable request.

Received: 26 April 2024; Accepted: 3 September 2025;
Published online: 20 November 2025

References

1. Kimble, H. J. The quantum internet. *Nature* **453**, 1023 (2008).
2. Wehner, S., Elkouss, D. & Hanson, R. Quantum internet: a vision for the road ahead. *Science* **362**, eaam9288 (2018).
3. Munro, W. J., Azuma, K., Tamaki, K. & Nemoto, K. Inside quantum repeaters. *IEEE J. Sel. Top. Quantum Electron.* **21**, 78 (2015).
4. Azuma, K. et al. Quantum repeaters: from quantum networks to the quantum internet. *Rev. Mod. Phys.* **95**, 045006 (2023).
5. Hermans, S. L. N. et al. Qubit teleportation between non-neighbouring nodes in a quantum network. *Nature* **605**, 663 (2022).
6. Knaut, C.M., Suleymanzade, A. & Wei, YC. et al. Entanglement of nanophotonic quantum memory nodes in a telecom network. *Nature* **629**, 573–578 (2024).
7. Heller, L., Farrera, P., Heinze, G. & de Riedmatten, H. Cold-atom temporally multiplexed quantum memory with cavity-enhanced noise suppression. *Phys. Rev. Lett.* **124**, 210504 (2020).
8. Pu, Y.-F. et al. Experimental demonstration of memory-enhanced scaling for entanglement connection of quantum repeater segments. *Nat. Photonics* **15**, 374 (2021).
9. Askarani, M. F. et al. Long-lived solid-state optical memory for high-rate quantum repeaters. *Phys. Rev. Lett.* **127**, 220502 (2021).
10. Bock, M. et al. High-fidelity entanglement between a trapped ion and a telecom photon via quantum frequency conversion. *Nat. Commun.* **9**, 1998 (2018).
11. Krutyanskiy, V. et al. Telecom-wavelength quantum repeater node based on a trapped-ion processor. *Phys. Rev. Lett.* **130**, 213601 (2023).
12. Kindem, J. M. et al. Control and single-shot readout of an ion embedded in a nanophotonic cavity. *Nature* **580**, 201 (2020).
13. Ourari, S. et al. Indistinguishable telecom band photons from a single Er ion in the solid state. *Nature* **620**, 977 (2023).
14. Neuwirth, J. et al. Quantum dot technology for quantum repeaters: from entangled photon generation toward the integration with quantum memories. *Mater. Quantum Technol.* **1**, 043001 (2021).
15. Sangouard, N., Simon, C., de Riedmatten, H. & Gisin, N. Quantum repeaters based on atomic ensembles and linear optics. *Rev. Mod. Phys.* **83**, 33 (2011).
16. Nemoto, K. et al. Photonic quantum networks formed from NV-centers. *Sci. Rep.* **6**, 26284 (2016).
17. Borregaard, J. et al. One-way quantum repeater based on near-deterministic photon-emitter interfaces. *Phys. Rev. X* **10**, 021071 (2020).
18. Sharman, K., Kimiaee Asadi, F., Wein, S. C. & Simon, C. Quantum repeaters based on individual electron spins and nuclear-spin-ensemble memories in quantum dots. *Quantum* **5**, 570 (2021).
19. Duan, L. M., Lukin, M. D., Cirac, J. I. & Zoller, P. Long-distance quantum communication with atomic ensembles and linear optics. *Nature* **414**, 413 (2001).
20. Lago-Rivera, D., Grandi, S., Rakonjac, J. V., Seri, A. & de Riedmatten, H. Telecom-heralded entanglement between multimode solid-state quantum memories. *Nature* **594**, 37 (2021).
21. Li, H. et al. Heralding quantum entanglement between two room-temperature atomic ensembles. *Optica* **8**, 925 (2021).
22. Businger, M. et al. Non-classical correlations over 1250 modes between telecom photons and 979-nm photons stored in 171yb3+:y2sio5. *Nat. Commun.* **13**, 6438 (2022).
23. Krovi, H. et al. Practical quantum repeaters with parametric down-conversion sources. *Appl. Phys. B* **122**, 52 (2016).
24. Yoshida, D. & Horikiri, T. Multiplexed quantum repeaters based on single-photon interference with mild stabilization. *Commun Phys* **7**, 367 (2024).
25. Langenfeld, S., Thomas, P., Morin, O. & Rempe, G. Quantum repeater node demonstrating unconditionally secure key distribution. *Phys. Rev. Lett.* **126**, 230506 (2021).
26. Morin, O., Körber, M., Langenfeld, S. & Rempe, G. Deterministic shaping and reshaping of single-photon temporal wave functions. *Phys. Rev. Lett.* **123**, 133602 (2019).
27. Knall, E. N. et al. Efficient source of shaped single photons based on an integrated diamond nanophotonic system. *Phys. Rev. Lett.* **129**, 053603 (2022).
28. Raha, M. et al. Optical quantum nondemolition measurement of a single rare earth ion qubit. *Nat. Commun.* **11**, 1605 (2020).
29. Kalb, N. et al. Entanglement distillation between solid-state quantum network nodes. *Science* **356**, 928 (2017).
30. Tanzilli, S. et al. A photonic quantum information interface. *Nature* **437**, 116 (2005).
31. Bhaskar, M. K. et al. Experimental demonstration of memory-enhanced quantum communication. *Nature* **580**, 60 (2020).
32. Wei, Y.-C. et al. Universal distributed blind quantum computing with solid-state qubits. *Science* **388**, 509 (2025).
33. Reiserer, A., Kalb, N., Rempe, G. & Ritter, S. A quantum gate between a flying optical photon and a single trapped atom. *Nature* **508**, 237 (2014).
34. Kalb, N., Reiserer, A., Ritter, S. & Rempe, G. Heralded storage of a photonic quantum bit in a single atom. *Phys. Rev. Lett.* **114**, 220501 (2015).
35. Beukers, H. K. et al. Remote-entanglement protocols for stationary qubits with photonic interfaces. *PRX Quantum* **5**, 010202 (2024).
36. Calsamiglia, J. & Lütkenhaus, N. Maximum efficiency of a linear-optical bell-state analyzer. *Appl. Phys. B* **72**, 67 (2001).
37. Li, L., Hu, X., Jia, Z. et al. Parallelized telecom quantum networking with an ytterbium-171 atomarray. Nat. Phys. (2025). https://doi.org/10.1038/s41567-025-03022-4
38. Zhang, Y., McCutcheon, M. W., Burgess, I. B. & Loncar, M. Ultra-high-q te/tm dual-polarized photonic crystal nanocavities. *Opt. Lett.* **34**, 2694 (2009).
39. Vučković, J., Rivoire, K. & Buckley, S. Multiply resonant photonic crystal nanocavities for nonlinear frequency conversion. *Opt. Express* **19**, 22198–22207 (2011).
40. Menon, S.G., Glachman, N. & Pompili, M. et al. An integrated atom array-nanophotonic chip platform with background-free imaging. *Nat Commun* **15**, 6156 (2024).
41. Kim, M. E., Chang, T.-H., Fields, B. M., Chen, C.-A. & Hung, C.-L. Trapping single atoms on a nanophotonic circuit with configurable tweezer lattices. *Nat. Commun.* **10**, 1 (2019).
42. Thompson, J. D. et al. Coupling a single trapped atom to a nanoscale optical cavity. *Science* **340**, 1202 (2013).

43. Samutpraphoot, P. et al. Strong coupling of two individually controlled atoms via a nanophotonic cavity. *Phys. Rev. Lett.* **124**, 063602 (2020).
44. McCutcheon, M. W. & Lončar, M. Design of a silicon nitride photonic crystal nanocavity with a quality factor of one million for coupling to a diamond nanocrystal. *Opt. Express* **16**, 19136 (2008).
45. Ye, Z., Fülöp, A., Helgason, Ó. B., Andrekson, P. A. & Torres-Company, V. Low-loss high-Q silicon-rich silicon nitride microresonators for Kerr nonlinear optics. *Opt. Lett.* **44**, 3326 (2019).
46. Debnath, K. et al. Ultrahigh-Q photonic crystal cavities in silicon rich nitride. *Opt. Express* **25**, 27334 (2017).
47. Schöll, E. et al. Crux of using the cascaded emission of a three-level quantum ladder system to generate indistinguishable photons. *Phys. Rev. Lett.* **125**, 233605 (2020).
48. Thompson, J. D., Tiecke, T., Zibrov, A. S., Vuletić, V. & Lukin, M. D. Coherence and Raman sideband cooling of a single atom in an optical tweezer. *Phys. Rev. Lett.* **110**, 133001 (2013).
49. Kaufman, A. M., Lester, B. J. & Regal, C. A. Cooling a single atom in an optical tweezer to its quantum ground state. *Phys. Rev. X* **2**, 041014 (2012).
50. Zhou, X., Tamura, H., Chang, T.-H. & Hung, C.-L. Trapped atoms and superradiance on an integrated nanophotonic microring circuit. *Phys. Rev. X* **14**, 031004 (2024).
51. Meng, Y., Dareau, A., Schneeweiss, P. & Rauschenbeutel, A. Near-ground-state cooling of atoms optically trapped 300 nm away from a hot surface. *Phys. Rev. X* **8**, 031054 (2018).
52. Lvovsky, A. I., Sanders, B. C. & Tittel, W. Optical quantum memory. *Nat. Photonics* **3**, 706 (2009).
53. Jing, B. & Bao, X.-H. Ensemble-based quantum memory: principle, advance, and application. *Photonic Quantum Technol. Sci. Appl.* **2**, 433 (2023).
54. Ma, L., Slattery, O. & Tang, X. Optical quantum memory based on electromagnetically induced transparency. *J. Opt.* **19**, 043001 (2017).
55. Bussiéres, F. et al. Prospective applications of optical quantum memories. *J. Mod. Opt.* **60**, 1519 (2013).
56. Afzelius, M., Simon, C., de Riedmatten, H. & Gisin, N. Multimode quantum memory based on atomic frequency combs. *Phys. Rev. A* **79**, 052329 (2009).
57. Jobez, P. et al. Towards highly multimode optical quantum memory for quantum repeaters. *Phys. Rev. A* **93**, 032327 (2016).
58. Bashkansky, M., Fatemi, F. K. & Vurgaftman, I. Quantum memory in warm rubidium vapor with buffer gas. *Opt. Lett.* **37**, 142 (2012).
59. Vernaz-Gris, P., Huang, K., Cao, M., Sheremet, A. S. & Laurat, J. Highly-efficient quantum memory for polarization qubits in a spatially-multiplexed cold atomic ensemble. *Nat. Commun.* **9**, 1 (2018).
60. Cho, Y.-W. et al. Highly efficient optical quantum memory with long coherence time in cold atoms. *Optica* **3**, 100 (2016).
61. Hosseini, M., Sparkes, B. M., Campbell, G., Lam, P. K. & Buchler, B. C. High efficiency coherent optical memory with warm rubidium vapour. *Nat. Commun.* **2**, 1 (2011).
62. Guo, J. et al. High-performance Raman quantum memory with optimal control in room temperature atoms. *Nat. Commun.* **10**, 1 (2019).
63. Tittel, W. et al. Photon-echo quantum memory in solid state systems. *Laser Photonics Rev.* **4**, 244 (2010).
64. Thiel, C., Böttger, T. & Cone, R. Rare-earth-doped materials for applications in quantum information storage and signal processing. *J. Lumin.* **131**, 353 (2011).
65. Zhong, T. & Goldner, P. Emerging rare-earth doped material platforms for quantum nanophotonics. *Nanophotonics* **8**, 2003 (2019).
66. Liu, G. & Jacquier, B. *Spectroscopic Properties of Rare Earths in Optical Materials* Vol. 83 (Springer Science & Business Media, 2006).
67. Preston, D. W. Doppler-free saturated absorption: laser spectroscopy. *Am. J. Phys.* **64**, 1432 (1996).
68. Sinclair, N. et al. Spectral multiplexing for scalable quantum photonics using an atomic frequency comb quantum memory and feed-forward control. *Phys. Rev. Lett.* **113**, 053603 (2014).
69. Puigibert, M. L. G. et al. Entanglement and nonlocality between disparate solid-state quantum memories mediated by photons. *Phys. Rev. Res.* **2**, 013039 (2020).
70. Böttger, T., Thiel, C., Sun, Y. & Cone, R. Optical decoherence and spectral diffusion at 1.5 μ m in Er^{3+}: Y_2SiO_5 versus magnetic field, temperature, and Er^{3+} concentration. *Phys. Rev. B* **73**, 075101 (2006).
71. Afzelius, M. & Simon, C. Impedance-matched cavity quantum memory. *Phys. Rev. A* **82**, 022310 (2010).
72. Davidson, J. H., Lefebvre, P., Zhang, J., Oblak, D. & Tittel, W. Improved light-matter interaction for storage of quantum states of light in a thulium-doped crystal cavity. *Phys. Rev. A* **101**, 042333 (2020).
73. Das, A., Davidson, J. H., Chakraborty, T., Tchebotareva, A. L. & Tittel, W. Towards an alignment-free, impedance-matched cavity quantum memory in a thulium-doped crystal. in *CLEO 2023* STh5C.6. https://doi.org/10.1364/CLEO_SI.2023.STh5C.6 (Optica Publishing Group, 2023).
74. Duranti, S. et al. Efficient cavity-assisted storage of photonic qubits in a solid-state quantum memory. *Opt. Express* **32**, 26884 (2024).
75. Sinclair, N., Oblak, D., Thiel, C. W., Cone, R. L. & Tittel, W. Properties of a rare-earth-ion-doped waveguide at sub-Kelvin temperatures for quantum signal processing. *Phys. Rev. Lett.* **118**, 100504 (2017).
76. Das, A. et al. Optical investigations of coherence and relaxation dynamics of a thulium-doped yttrium gallium garnet crystal at sub-kelvin temperatures for optical quantum memory. *Mater. Quantum Technol.* **4**, 035202 (2024).
77. Sun, Y., Thiel, C. & Cone, R. Optical decoherence and energy level structure of 0.1% tm 3+: Linbo 3. *Phys. Rev. B* **85**, 165106 (2012).
78. Sinclair, N. et al. Optical coherence and energy-level properties of a TM 3+-doped li nb o 3 waveguide at subkelvin temperatures. *Phys. Rev. B* **103**, 134105 (2021).
79. Saglamyurek, E. et al. Conditional detection of pure quantum states of light after storage in a TM-doped waveguide. *Phys. Rev. Lett.* **108**, 083602 (2012).
80. McAuslan, D., Bartholomew, J., Sellars, M. & Longdell, J. J. Reducing decoherence in optical and spin transitions in rare-earth-metal-ion-doped materials. *Phys. Rev. A* **85**, 032339 (2012).
81. Davidson, J. H. et al. Measurement of the thulium ion spin hamiltonian in an yttrium gallium garnet host crystal. *Phys. Rev. B* **104**, 134103 (2021).
82. Thiel, C. W., Babbitt, W. R. & Cone, R. L. Optical decoherence studies of yttrium oxyorthosilicate Y_2SiO_5 codoped with Er^{3+} and Eu^{3+} for optical signal processing and quantum information applications at 1.5 microns. *Phys. Rev. B* **85**, 174302 (2012).
83. Böttger, T., Thiel, C. W., Cone, R. L. & Sun, Y. Controlled compositional disorder in Er^{3+}: Y_2SiO_5 provides a wide-bandwidth spectral hole burning material at 1.5μm. *Phys. Rev. B* **77**, 155125 (2008).
84. Thiel, C. W., Sinclair, N., Tittel, W. & Cone, R. L. Optical decoherence studies of Tm^{3+}:$Y_3Ga_5O_{12}$. *Phys. Rev. B* **90**, 214301 (2014).
85. Ferrier, A., Ilas, S., Goldner, P. & Louchet-Chauvet, A. Scandium doped TM: YAG ceramics and single crystals: coherent and high resolution spectroscopy. *J. Lumin.* **194**, 116 (2018).
86. Zhang, Z. et al. Tailoring the $^3F_4$ level lifetime in Tm^{3+}:$Y_3Al_5O_{12}$ by Eu^{3+} co-doping for signal processing application. *J. Lumin.* **222**, 117107 (2020).
87. Bennett, C. H. & Brassard, G. Quantum cryptography: public key distribution and coin tossing. *Theor. Comput. Sci.* **560**, 7 (2014).

88. Lo, H.-K., Chau, H. F. & Ardehali, M. Efficient quantum key distribution scheme and a proof of its unconditional security. *J. Cryptol.* **18**, 133 (2005).
89. Scarani, V. et al. The security of practical quantum key distribution. *Rev. Mod. Phys.* **81**, 1301 (2009).
90. Welte, S., Hacker, B., Daiss, S., Ritter, S. & Rempe, G. Photon-mediated quantum gate between two neutral atoms in an optical cavity. *Phys. Rev. X* **8**, 011018 (2018).
91. Welte, S. et al. A nondestructive Bell-state measurement on two distant atomic qubits. *Nat. Photonics* **15**, 504 (2021).
92. Grinkemeyer, B. et al. Error-detected quantum operations with neutral atoms mediated by an optical cavity. *Science* **387**, 1301 (2025).
93. Huber, D., Reindl, M., Aberl, J., Rastelli, A. & Trotta, R. Semiconductor quantum dots as an ideal source of polarization-entangled photon pairs on-demand: a review. *J. Opt.* **20**, 073002 (2018).
94. Heller, L., Lowinski, J., Theophilo, K., Padrón-Brito, A. & de Riedmatten, H. Raman storage of quasideterministic single photons generated by Rydberg collective excitations in a low-noise quantum memory. *Phys. Rev. Appl.* **18**, 024036 (2022).
95. Guo, M. et al. Rare-earth quantum memories: the experimental status quo. *Front. Phys.* **18**, 21303 (2023).
96. Tchebotareva, A. et al. Entanglement between a diamond spin qubit and a photonic time-bin qubit at telecom wavelength. *Phys. Rev. Lett.* **123**, 063601 (2019).
97. Iuliano, M. et al. Interfacing an NV-center in diamond and a rare-earth ion compatible photonic time-bin qubit. In *Proc. Optica Quantum 2.0 Conference and Exhibition* QW4A.7. https://doi.org/10.1364/QUANTUM.2023.QW4A.7 (Optica Publishing Group, 2023).
98. Jiang, N. et al. Experimental realization of 105-qubit random access quantum memory. *npj Quantum Inf.* **5**, 28 (2019).
99. Quan, Q. & Loncar, M. Deterministic design of wavelength scale, ultra-high Q photonic crystal nanobeam cavities. *J. Opt. Soc. Am. A* **424**, 435 (2003).
100. Goban, A. et al. Atom-light interactions in photonic crystals. *Nat. Commun.* **5**, 1 (2014).
101. Philipp, H. R. Optical properties of silicon nitride. *J. Electrochem. Soc.* **120**, 295 (1973).
102. Menon, S. G., Singh, K., Borregaard, J. & Bernien, H. Nanophotonic quantum network node with neutral atoms and an integrated telecom interface. *New J. Phys.* **22**, 073033 (2020).
103. Gu, F. Codes underlying the publication: “hybrid quantum repeaters with ensemble-based quantum memories and single-spin photon transducers”. https://doi.org/10.4121/589448ac-1be7-43a7-988d-c4c1122eb4e8.v1 (2024).

Acknowledgements

J.B. and F.G. acknowledge funding from the NWO Gravitation Program Quantum Software Consortium (Project QSC No. 024.003.037). J.B. acknowledges support from the AWS Quantum Discovery Fund at the Harvard Quantum Initiative. H.B. and S.G.M. gratefully acknowledge funding from the NSF QLCI for Hybrid Quantum Architectures and Networks (NSF award 2016136), and the NSF Quantum Interconnects Challenge for Transformational Advances in Quantum Systems (NSF award 2138068). W.T. acknowledges funding through the Netherlands Organization for Scientific Research and the European Union’s Horizon 2020 Research and Innovation Program under Grant Agreement No. 820445 and Project Name Quantum Internet Alliance, as well as from the Swiss State Secretariat for Education, Research and Innovation (SERI) under contract number UeM019-3.

Author contributions

F.G. performed the numerical analysis of the Rb entangled photon source. F.G. and D.M. performed the numerical optimization of the full repeater chain. S.G.M. made the nanocavity design and the numerical simulation of its characteristics. A.D., T.C., and W.T. performed the experimental validation of the compatibility of the visible photon with a Tm-memory. W.T., H.B., and J.B. envisioned and supervised the project. All authors contributed to the writing of the manuscript.

Competing interests

The authors declare no competing interests.

Additional information

Supplementary information The online version contains supplementary material available at https://doi.org/10.1038/s41534-025-01119-5.

Correspondence and requests for materials should be addressed to Johannes Borregaard.